HHS Public Access

Author manuscript

J Neural Eng. Author manuscript; available in PMC 2023 September 11.

Published in final edited form as:

J Neural Eng. ; 18(4): . doi:10.1088/1741-2552/ac1984.

Thin-film microfabrication and intraoperative testing of μECoG and iEEG depth arrays for sense and stimulation

Kristin K Sellers[1,3,*], **Jason E Chung**[1,3], **Jenny Zhou**[2], **Michael G Triplett**[2], **Heather E Dawes**[1], **Razi Haque**[2], **Edward F Chang**[1]

[1]Department of Neurological Surgery, Weill Institute for Neurosciences, University of California San Francisco, San Francisco, CA, United States of America

[2]Lawrence Livermore National Laboratories, Livermore, CA, United States of America

[3]These authors contributed equally.

Abstract

Objective.—Intracranial neural recordings and electrical stimulation are tools used in an increasing range of applications, including intraoperative clinical mapping and monitoring, therapeutic neuromodulation, and brain computer interface control and feedback. However, many of these applications suffer from a lack of spatial specificity and localization, both in terms of sensed neural signal and applied stimulation. This stems from limited manufacturing processes of commercial-off-the-shelf (COTS) arrays unable to accommodate increased channel density, higher channel count, and smaller contact size.

Approach.—Here, we describe a manufacturing and assembly approach using thin-film microfabrication for 32-channel high density subdural micro-electrocorticography (μECoG) surface arrays (contacts 1.2 mm diameter, 2 mm pitch) and intracranial electroencephalography (iEEG) depth arrays (contacts 0.5 mm 1.5 mm, pitch 0.8 mm × 2.5 mm). Crucially, we tackle the translational hurdle and test these × arrays during intraoperative studies conducted in four humans under regulatory approval.

Main results.—We demonstrate that the higher-density contacts provide additional unique information across the recording span compared to the density of COTS arrays which typically have electrode pitch of 8 mm or greater; 4 mm in case of specially ordered arrays. Our intracranial stimulation study results reveal that refined spatial targeting of stimulation elicits evoked potentials with differing spatial spread.

*Author to whom any correspondence should be addressed. kristin.sellers@ucsf.edu.

Author contributions

K K S, H E C, R H, and E F C conceived of and designed the study; K K S and E F C collected the data; J Z, M G T, and R H designed and manufactured the arrays; K K S and J E C analyzed the data. K K S, J E C, J Z, M G T, R H wrote the manuscript; H E D and E F C supervised the work. All authors approved of the final manuscript.

Ethical Statement

Written informed consent was obtained from all study participants. All studies were carried out in accordance with ethical policies, approved by the IRB at the University of California, San Francisco (protocol #14–15 341).

Significance.—Thin-film, μECoG and iEEG depth arrays offer a promising substrate for advancing a number of clinical and research applications reliant on high-resolution neural sensing and intracranial stimulation.

Keywords

μECoG; iEEG; intracranial stimulation; microfabrication; thin-film arrays; human; intraoperative

1. Introduction

Direct brain recordings conducted on the subdural surface of the brain (electrocorticography, ECoG) or in subsurface structures (intracranial electroencephalography, iEEG) provide high temporal resolution of local population activity. This neural activity is useful for a variety of diagnostic and therapeutic purposes, including epilepsy seizure localization [1–3] and control of brain–computer interface (BCI) systems for cursor movement [4] or prosthetic limbs [5]. In addition to sensing neural activity, intracranial electrical stimulation can be applied through these electrodes for a variety of applications. Implanted devices deliver stimulation for the treatment of Parkinson's Disease and other movement disorders [6], neuropsychiatric diseases [7], and for the prevention of seizures [8]; intracranial stimulation is also well-established in the intraoperative setting to guide surgical decision-making [9]. Closed-loop intracranial stimulation has shown promise as a therapy for a number of diseases [10, 11], which relies on sensing neural activity, calculating a symptom biomarker, and delivering stimulation based on the real-time sensed status of the symptom biomarker.

However, many of these applications suffer in performance and utility in humans because of the large electrode sizes and low electrode density in FDA-cleared, commercial-off-the-shelf (COTS) electrode arrays, despite the availability of a variety of designs. Subdural surface arrays have 4–64 contacts, with electrode diameters of 2–4 mm, and center-to-center electrode spacing of 8–10 mm; iEEG depth arrays have 4–16 contacts along the *z*-axis with spacing of 5–10 mm. COTS arrays are typically manufactured in a highly manual fashion using bulk electrode materials and discrete wires to form electrical connections. In COTS surface arrays, individual platinum disc electrodes are embedded in a polymer substrate, typically silicone, to form the body of the array. In COTS depth arrays, discrete platinum ring electrodes are bonded to a polymer tube to form the array body. These manufacturing steps are not able to meet the demand for higher density arrays with smaller electrodes [12]. More recently, commercial entities have started employing advanced solutions to address these challenges with newer materials and manufacturing processes. CorTec has received FDA 510(k) clearance for sub-chronic (<30 d implant) 64-contact grids manufactured using a proprietary laser-assisted process. The arrays have 10 mm electrode spacing and are made with 90:10 platinum:iridium electrodes on silicone substrate with or without paralyene-C on top. CorTec is also manufacturing higher density arrays for preclinical research (not FDA cleared) with 8–32 contacts, with contact size as small as 0.2 mm and contact spacing as small as 0.9 mm. NeuroOne has received FDA 510(k) clearance for cortical thin-film electrodes containing 2–16 electrodes with 10 mm contact spacing and 3 mm contact size. The electrodes are platinum with a polyimide electrode substrate material.

Taking a microfabrication approach can bypass many of the scalability issues seen in traditional manufacturing methods. Thin-film microfabrication techniques offer unmatched control over device shape and feature size, down to the micron scale, while taking advantage of wafer-level processing. The hands-off nature of this approach coupled with its precise control over feature and device geometry enables the manufacture of devices with increased electrode density for high resolution sensing and stimulation [13] while maintaining a final footprint similar to that of COTS devices. Furthermore, microfabrication enables bulk processing in which multiple devices can fit on a single carrier substrate and all devices undergo identical conditions, thereby improving electrode-to-electrode and device-to-device uniformity and reproducibility. Such polyimide-based devices have been fabricated in the past with single layer metal traces [14–16] while the work here takes this further by introducing multiple layers, thus increasing the maximum electrode density over previous studies.

Testing of higher density, traditionally fabricated ECoG arrays in humans has demonstrated improved performance or spatial resolution over standard density COTS arrays. ECoG-based BCI performance of a multi-degree-of-freedom prosthetic arm was improved by higher density arrays (2 mm diameter, 4 mm pitch) over conventional arrays (4 mm diameter, 10 mm pitch) [17]. Comparison across patients with a standard size ECoG grid with 10 mm pitch, μECoG grid with 1 or 2 mm pitch, and a penetrating multielectrode array showed the activity recorded using the μECoG array was more similar to that from the penetrating array than the standard size ECoG grid in terms of correlation, coherence, and phase-locking/phase lag index across all electrode pairs in the array [18]. Recordings using 4 mm pitch arrays showed that neural activity during speech-task-responsive adjacent contacts was not highly correlated, particularly in the higher frequency bands [19], indicating that unique information is encoded and represented at this spatial scale.

Research studies, primarily conducted in animal models, have developed and tested high-density, thin-film arrays and demonstrated their utility. Chiang *et al* utilized a combination of multiple high-density μECoG arrays for a total of 294 contacts (229 μm diameter, 610 μm pitch) during an NHP auditory decoding task to improve decoding accuracy through optimizing channel sub-selection [20]. In a NHP study using 96-channel surface arrays (350 μm^2 electrode area, 700 μm pitch), use of all channels provided greater prediction accuracy in determining which finger was electrically stimulated from recorded somatosensory evoked potentials; the authors found increased spatial resolution of the high density array was less useful for low-frequency band signatures [21]. Limited studies of thin-film surface arrays in humans for research purposes show the utility of higher density contacts for localizing responses to stimuli [13]. However, there has largely been a gap in the translation of these thin-film high-density research devices to clinical and therapeutic use in humans.

Poly(3,4-ethylenedioxythiophene) (PEDOT), a conducting polymer, is also increasingly being used as a coating on metal electrodes for high density electrode arrays; PEDOT is often doped with polystyrene sulfonate (PEDOT:PSS) to provide superior impedance and charge-transfer capacity properties [22]. However, PEDOT:PSS coatings can suffer from cracks and delaminate from their metallic substrates during prolonged periods of charge-balanced biphasic electrical stimulation [23]. Additional manufacturing processes (such as

surface roughening) improve coating lifetime [22, 24, 25] and work is continuing to improve the lifetime of PEDOT:PSS. However, with an eye towards rapid translation to clinical and research use, we sought to use alternative materials, such as co-deposited platinum-iridium which does not require additional surface processing and still provides lower impedance and higher charge-transfer capacity properties compared to an untreated platinum surface.

Here, we microfabricated and assembled flexible 32-channel electrode arrays capable of simultaneous sense and stimulation. We tested the sense and stimulation capability of these surface and depth arrays intraoperatively in four human patients, using metrics applicable to clinical diagnostics and treatment (correlation across contacts and single-pulse stimulation (SPS) to measure corticocortical evoked potentials (CCEPs)). These higher-density μECoG and iEEG arrays provided more unique recorded information, evidenced by correlation coefficients lower than 1 between adjacent contacts, and stimulation evoked responses differing in spatial profile as a function of the location of the bipolar electrode pair used to deliver current. Together, this shows the feasibility and utility in manufacturing higher density arrays for human clinical and research needs.

2. Methods

2.1. Materials

Materials intended to be in contact with tissue were carefully chosen for their biocompatibility (table 1). These materials, as well as consumables such as cleaning solvents and intermediate materials, were evaluated as part of the completed, finished device. In order to acquire regulatory approvals for the intended intraoperative use-case, biocompatibility studies were used to determine suitability for implantation. These tests were conducted by a third-party testing laboratory that follows specific protocols in accordance with regulatory requirements (e.g. ISO 10993). All fabricated devices that were used in humans have passed such testing conducted by Toxikon Corporation.

2.2. Array design

Surface and depth arrays contained 32 channels in a grid, with 8 rows and 4 columns of primary electrodes (figure 1(a)). For surface arrays, the primary electrodes were 1.2 mm in diameter with 2 mm pitch (here and throughout, pitch refers to electrode center-to-center spacing). Total recording span was 15.2 mm × 7.2 mm. For depth arrays, the grid was ‘wrapped’ around a cylinder such that the eight rows spanned the z direction. The primary electrodes were 1.5 mm × 0.5 mm in size, spaced 1 mm edge-to-edge axially and 0.301 mm edge-to-edge circumferentially. Total recording span was 19 mm. Separate ground and reference electrodes were positioned on the periphery of the array (surface) or proximally (depth array).

2.3. Array fabrication

The surface and depth arrays were fabricated using standard microfabrication techniques [28] with a six-mask photolithographic process where each six inch silicon carrier wafer contained twelve 32-channel arrays (figure 1(b)). All arrays consist of two metal trace layers encapsulated between insulative layers of polyimide [28] with exposed platinum iridium

electrodes (figures 1(c) and (d)). The fabrication process steps are illustrated in figure 1(e). First, two layers of polyimide (PI-2611, HD MicroSystems) were spin-coated and cured at a final temperature of 375 °C for 30 min on the silicon carrier wafer to achieve a total thickness of 10 μm. Polyimide is a proven biocompatible and chemically inert material that is easily patterned using standard photolithographic and plasmaetching processes [29]; it provides a mechanically flexible device platform which can be manipulated into three-dimensional (3D) shapes.

Next, the first metal stack was sputter-deposited and patterned using a plasma etch process. This process uses both physical (ion-bombardment) and chemical etch process to remove material. A second 10 μm layer of polyimide was then deposited to insulate the patterned metal from the previous step. Interconnection vias were patterned and etched on this polyimide layer, so the next metal layer could make electrical contact with the metal layer below. After the second layer of metal was deposited, the top layer of titanium from the metal stack was removed at the electrode and connector sites via a chemical etch process in diluted hydrofluoric acid to expose the PtIr metal and then patterned. The last 10 μm layer of polyimide was spin-coated and cured. Finally, polyimide covering the electrode and connector sites and the device outline was patterned. The process wafers with 30 μm thick polyimide-based arrays were then soaked in warm deionized water before device release.

Each trace metal layer consisted of a 2.04 μm thick Ti/PtIr/Au/PtIr/Ti metal stack with the top titanium layer, on the second metal layer, etched to expose the 0.25 μm thick co-sputtered platinum iridium contacts below. Three-quarters of the metal trace layer thickness was gold, which both helped to reduce electrical trace resistance down to 140–240 Ω and provided a malleable and ductile material to prevent defects and facilitate coiling and formation of the array into 3D shapes during the device assembly process.

The platinum-iridium layer served both as the active electrode surface and the diffusion barrier between titanium and gold to prevent interdiffusion, which can lead to increased trace resistance. Titanium-gold interdiffusion occurs at temperatures in the range of 250 °C to 325 °C [30–32], which is below the polyimide cure temperature used in the fabrication process. Without a barrier layer of platinum-iridium, this interdiffusion results in measurably higher resistivity in the trace metal. Since high-density arrays require smaller electrodes, signal-to-noise (SNR) ratio typically decreases because of increased electrode impedance [12, 33]. To maintain sufficient SNR and increase electrode charge storage capacity and charge injection efficiency for stimulation, deposition parameters for the PtIr metal electrode were optimized to provide low impedance, high charge-storage capacitance and high double-layer capacitance without requiring post-fabrication surface modifications. Untreated thin-film Pt is reported to have a double-layer capacitance (Q) of 0.01–0.06 mF cm^{-2} [25, 34] while post-processed surface roughening of thin-film Pt contacts achieved a Q of 2 mF cm^{-2}, or approximately 40 times higher than that of untreated Pt film [25]. The co-sputter process developed here (60% Pt and 40% Ir) resulted in a measured Q of approximately 3.1 mF cm^{-2}, at least 50 times increase without post-processing when fit with the same model. In comparison, the Q of co-sputter deposited PtIr is 1.5 times greater than that of electrodeposited 60%–40% PtIr alloy [35].

2.4. Array assembly

Once the microfabricated arrays were removed from the wafer, the devices were ball-bonded to an interface board with one end connected to the array and the other connected to a 36-channel Omnetics connector for intraoperative testing (figure 2). The Omnetics connector could easily be substituted with a different connector to facilitate connection to data acquisition and stimulation equipment. The ball-bonded connection was encapsulated with biocompatible epoxy (EpoTek 301–2, Epoxy Technology Inc.) to provide mechanical stability. Surface arrays were attached to a silicone support tube (AlliedSil Silicone Tubing — Implant Grade, Implantech) and the cable region of the device was wrapped helically around the support tube. The coiled subassembly was placed into a polycarbonate mold and over-molded with silicone (Nusil MED-6215, Avantor, Inc). The silicone coat holds the coiled cable in place and provides mechanical support for the electrode region of the device. The support tube, which accepts a stainless steel stylet, runs the full length of the device, including behind the electrode region, to allow the surgeon to steer the array into regions of the brain not easily accessed without increasing the size of the craniotomy. Once over-molded in silicone, the interface board was over-molded in biocompatible epoxy (EpoTek 301–2FL, Epoxy Technology, Inc).

For the depth arrays, the assembly process differed slightly following ball-bonding to the interface board (figure 2). The electrode region was formed into a cylinder to take the shape of a typical depth probe. The depth arrays were pre-formed into a ‘U’ shape by heating the electrode region of the array to 260 °C and pressing it into a stainless-steel mold, electrode side down. To protect the electrodes from abrasion, a thin sheet of polyimide, 10 μm thick, was placed between the electrode array and the stainless-steel mold during the pre-forming process. The pre-formed array was temporarily bonded to a thermoplastic polyurethane (TPU) support tube (Carbothane TPU PC-3585 A, Lubrizol Corporation) using a small amount of UV-cure adhesive (Loctite 4310, Henkel Corporation) applied at the pointed tip of the electrode array. The sub-assembly was pulled into a polytetrafluoroethylene (PTFE) mold and heated to 150 °C to permanently bond the electrode region of the array to the TPU support tube. At this point, the thin sheet of polyimide and pointed tip of the electrode array were removed, and UV-cure adhesive (Loctite 4310) was used to form a rounded tip at the distal end of the device to enable blunt dissection of tissue during insertion. Next the cable region of the array was helically wrapped around the support tube and over-molded in silicone (Nusil MED-6215) using a polycarbonate mold. As with the surface array, once over-molded in silicone, the interface board was over-molded in biocompatible epoxy (EpoTek 301–2FL). All design, fabrication, and assembly were conducted under a Quality Management System and with design controls, to enable rapid translation to human clinical applications [36].

2.5. Data collection

The experimental protocol was approved by the University of California, San Francisco Institutional Review Board. Four participants were included in the study (table 2) and all provided written informed consent. Surface arrays were tested in three patients (LA08, LA10, LA11) and depth arrays were tested in three patients (LA10, LA11, LA12). All patients had medically-refractory seizures requiring surgical management due to temporal

lobe epilepsy. Stimulation and recording were conducted in the operating room, using the 32-contact μECoG and/or iEEG depth arrays described above. Surface arrays (figures 2(h), 3(a) and (b)) were placed on the cortical surface following durotomy, and depth arrays (figures 2(g) and 3(a)) were inserted into healthy tissue that was scheduled to be removed later in the surgery due to clinically-indicated need to access epileptic tissue. Data acquisition and stimulation were conducted using a Neuro Omega (Alpha Omega) system sampled at 22 kHz (LA08, LA10, LA11) or a Tucker Davis Technologies system (PZ5M-512 and RZ2) sampled at 24.4 kHz (LA12). The Neuro Omega system has ±23 mV dynamic range and 16-bit resolution, and the TDT has ±500 mV dynamic range and 28-bit resolution, each enabling rapid signal recovery following delivery of stimulation. Reference and ground contacts built into the arrays were used for all recordings. The array was connected to the Neuro Omega headbox modules or TDT S-boxes using an Omnetics connector terminating in touch-proof connectors, connected to touchproof extenders to provide sufficient distance out of the sterile surgical field. The arrays, Omnetics-to-touchproof cable, and touchproof extenders were all sterilized using ethylene oxide prior to use.

2.6. Electrode stimulation

All electrical stimulation was delivered below accepted current density limits (30 $\mu C\ cm^{-2}$) [37] and using charge-balanced biphasic pulses (zero inter-phase delay) to ensure safety. SPS was delivered between bipolar contacts on surface arrays, selected at two distances from each other (referred to as varying proximities)—4 mm and 10 mm center-to-center distances. SPS was delivered with the following parameters: blocks of 10–30 s duration, 1 Hz, 400us pulsewidth, and 0.68 mA. Blocks of SPS were alternated with recording at rest (no stimulation) or other stimulation tests. A live stream of recordings was monitored during stimulation to check for stimulation-induced after-discharges (which may indicate that tissue is seizure prone if stimulation is continued), which were not seen in any of the participants. For LA10, the stimulation experiments were conducted while the participants were under anesthesia. For LA11, the stimulation experiments were conducted when the participant had been woken up during surgery and was resting quietly. No other sensory stimuli or tasks were co-administered during electrical stimulation.

2.7. Signal processing

Offline analyses were conducted using custom scripts in MATLAB (Mathworks, Inc. Natick, MA). Electrodes which were known to be shorted or open (based on impedance values measured in saline, prior to intraoperative testing) were excluded from all analyses. These excluded channels included LA08: channel 16, surface array; and LA12: channels 19 and 26, depth array. For resting-state correlation analyses, the following preprocessing was conducted: data were bandpass filtered from (2 250)Hz using a fourth order zero-phase butterworth filter; common average referencing; notch filtering at 60 Hz and harmonics using a fourth order zero-phase butterworth filter; downsampling to 512 Hz. When analyzing stimulation data, the electrode contacts used to deliver stimulation were excluded from analysis, as no recoverable neural sense data was present on these contacts. The following processing was conducted to calculate stimulation-evoked potentials: each SPS pulse was identified in the raw data using peak detection; a segment of data (typically 13 ms total) was

removed around that stimulation time to remove stimulation artifact and was replaced with generated data using a cubic spline interpolation [38]; data were bandpass filtered from [1 100] Hz using a fourth order zero-phase butterworth filter; 60 Hz line noise was removed using a fourth order zero-phase butterworth filter. Separately for each block of stimulation, the data were then segmented into trials (one trial = one biphasic stimulation pulse) with 500 ms of data prior to the stimulation pulse and 500 ms after the stimulation pulse. On a trial-by-trial and electrode-by-electrode basis, the preprocessed voltage data were z-scored −300 to −100 ms relative to the stimulation pulse start. Following these calculations, the period previously identified as stimulation was replaced with nans.

2.8. Quantification and statistical analysis

In order to ascertain if electrode contacts on arrays with this pitch recorded unique information, we calculated Pearson correlation coefficients on resting state data. Correlations were calculated between the preprocessed time series of all electrode pairs on data segments of 7–42 s in length. Prior studies have found that activity during resting state recordings was more highly correlated across electrodes compared to activity evoked by sensory stimulation or task [19], so the combination of this experimental paradigm and analysis represents a challenging scenario. We calculated the Euclidean distance between the electrode pairs, and each participant's data were fit to a Lorentzian regression model (1) with correlation is a function of distance:

$$y = (1 - c)\frac{B^2}{B^2 + x^2} + c\,. \tag{1}$$

We next asked if more refined spatial control of stimulation delivery, using the μECoG surface arrays, changed stimulation-evoked responses. For each subject and recording electrode, the voltage peak induced by SPS was taken from the 200 ms following stimulation of each trial. This peak voltage values were paired with the center-to-center distance of the closest stimulation electrode and then fit to a power regression model (2) where voltage peak is a function of center-to-center distance from the closest electrode:

$$y = A * X^b\,.$$

3. Results

We microfabricated and assembled subdural surface μECoG and iEEG depth arrays for human use with 2 mm and 0.8 mm 2.5 mm pitch, respectively. Our intraoperative sense and stimulation studies conducted in four human patients demonstrated that these higher density arrays provided additional sensed information and greater control over the spatial spread of stimulation. To quantify the similarity of the recorded signals, the relationship between pairwise center-to-center contact distance and signal correlation was fit using a Lorentzian regression model for each participant (1) using methodology similar to that reported previously [13]. As expected, the models fit well for surface arrays (LA08 R^2 =

0.6360; LA10 R^2 = 0.3554; LA11 R^2 = 0.4023) and depth arrays (LA10 R^2 = 0.4422; LA11 R^2 = 0.3695; LA12 R^2 = 0.4947) (figure 4).

Signals between adjacent contacts in the same row or column of the surface array, with 2 mm pitch, had correlation coefficients lower than 1, indicating that even during highly correlated resting state activity, this density of electrodes recorded unique information. However, it was not clear if even higher density electrodes would also provide meaningfully different signal. To address this, we took advantage of the grid design of the surface arrays and compared correlations between adjacent contacts in the same row or column (2 mm pitch) and diagonally adjacent contacts (2.83 mm pitch) (figure 4(a)). Interestingly, pairwise correlations differences between these sub-millimeter electrode spacings were highly significant in all participants (Wilcoxon rank-sum p-value, pairwise electrode distance 2 mm versus 2.83 mm: LA08 $p < 8.99 \times 10^{-8}$, LA10 $p < 2.93\ 10^{-5}$, LA11 $p < 2.17 \times 10^{-9}$), providing further ×evidence that sub-millimeter pitch μECoG arrays would provide unique information even when applied to human intraoperative recording.

We conducted a similar analysis for the depth arrays, taking into account their 3D geometry. These arrays have four recording contacts at the same insertion depth (figure 4(b), top), distributed around the cylinder of the full assembly. With this configuration, the electrodes at the same depth of insertion are a cord center-to-center distance of 0.7 mm (0.8 mm around the cylinder, on the array~surface) for neighboring electrodes, and a cord center-to-center pacing of 1 mm spacing for the next closest contact (the diameter of the cylinder). At this submillimeter difference in spacing (adjacent electrodes at the same depth, ~0.7 mm, and electrodes on the other side of the 3D structure, 1 mm), one of the three subjects tested had a significant correlation difference (p-value for Wilcoxon rank-sum at the same depth or within same axial ring, pairwise electrode distance ~0.7 mm versus 1 mm: LA10 $p <$ 0.022, LA11 $p < 0.121$, LA12 $p < 0.06$). Next, the pairwise correlation between contacts at the same depth were compared to those at adjacent depth. As described above, contacts at the same depth have center-to-center differences between ~0.7 mm and mm, while those at different depths have a ~1 cord center-to-center distance of 2.5 mm to ~2.7 mm. Pairwise correlations were significantly different between electrodes at different depths among all participants (p-value for Wilcoxon rank-sum between contacts of neighboring insertion depths, pairwise electrode distance ⩽1 mm versus 2.5 mm to 2.7 mm: LA10 $p < 4.64\ 10^{-9}$, LA11 $p < 0.0023$, LA12 p < 3.57 ×× 10^{-5}). This demonstrates that depth arrays with this pitch, and even smaller pitch, are effective at recording different information on adjacent contacts.

We next sought to investigate if more refined spatial delivery of stimulation changed evoked responses. The area of activated tissue is in part a function of the position and proximity of the two stimulation electrodes. SPS was delivered at electrodes with 4 mm or 10 mm center-to-center spacings with simultaneous recording from the other electrodes on the array (figure 5). The stimulation-evoked voltage peaks were largest on the contacts closest to either stimulation electrode with a drop-off increasing with distance from either electrode.

There were significant differences in the SPS evoked potential peak amplitudes, even when comparing the closest recorded electrodes (2 mm, horizontal or vertical, versus 2.83

mm, diagonal) across all participants and stimulation proximities (all p-values reported for Wilcoxon rank-sum: LA10 10 mm center-to-center spacing, $p < 1.72 \times 10^{-14}$, LA11 10 mm center-to-center spacing, $p < 3.14 \times 10^{-64}$; LA10 4 mm center-to-center spacing, $p < 1.00 \times 10^{-9}$; LA11 4 mm center-to-centerspacing, $p < 2.12 \times 10^{-64}$).

The drop-off of stimulation evoked peak over center-to-center distance from the closest stimulation electrode for every subject and every stimulation electrode spacing was fit to a power regression model (2). Power regression models fit better for participant LA11 and for larger center-to-center spacings (LA10 10 mm center-to-center spacing, $R^2 = 0.17$, LA11 10 mm center-to-center spacing, $R^2 = 0.45$; LA10 4 mm center-to-center spacing, $R^2 = 0.06$; LA11 4 mm center-to-center spacing, $R^2 = 0.40$) (figure 6), suggesting that many factors, such as local biological architecture, may heavily influence the evoked potentials from electrical stimulation. Taken together, these results demonstrate that higher spatial specificity of delivered electrical current afforded by μECoG indeed influences the tissue activated, and thus the evoked responses.

4. Discussion

The use of ECoG for diagnostic and therapeutic sensing and stimulation in humans has been hampered by the relatively low density and large contact size found in existing COTS arrays. Prior studies in animal models using higher-density research arrays have demonstrated improved decoding performance and sensitivity through the use of these higher channel count arrays [20, 21]. However, current manufacturing practices used for COTS arrays preclude continued miniaturization and increased density of electrode contacts. One way to bypass many of the scalability issues seen in traditional manufacturing methods is to use microfabrication. Fundamentally, microfabrication is a 2.5D process by which materials, such as metals ceramics, or polymers, are deposited onto a carrier substrate, typically silicon, in a layer-by-layer fashion. These materials are then patterned via photo-lithography and selectively etched to form functional devices. Microfabrication techniques allow for control over device shape and feature size, down to the micron scale, and allow for bulk wafer level processing where multiple devices can be processed simultaneously on a single carrier wafer. Since devices on the same carrier wafer undergo identical processing conditions, they exhibit excellent electrode-to-electrode and device-to-device consistency. Here, we described the manufacture, assembly, and human intraoperative testing of microfabricated thin-film surface and depth electrode arrays. The higher density arrays provided increased spatial specificity and precision for both sensing and stimulation.

4.1. Advantages of thin-film microfabrication

Surface and depth electrode arrays manufactured using thin-film microfabrication provide a number of advantages over currently available COTS arrays. The precision of the manufacturing process allows for higher channel count, greater density, and smaller contact size. The surface array described here (32 electrodes, 1.2 mm in diameter, 2 mm pitch) has an electrode density that is 4–25 times greater than commonly available COTS subdural surface arrays. The cylindrical depth array (32 rectangular electrodes, 0.5 mm circumferentially and 1.5 mm axially, 2.5 mm pitch axially and 0.8 mm pitch

circumferentially) has an electrode density that is 3.5–16 times higher than commonly available COTS depth arrays. While we manufactured and tested 32-channel arrays in the present study, the described microfabrication procedure can be scaled to make individual arrays with upwards of hundreds of channels and contact sizes down to 15 μm and 26 μm pitch, respectively. Currently, these high-density and high-channel count arrays are limited by the number of connections needed to interface with supporting electronics, rather than the microfabrication process itself. Thin-film arrays also have multiple mechanical properties that facilitate high signal quality. The microfabricated surface arrays consist of a 30 μm layer of polyimide encased in a 750 μm layer of silicone, approximately the same thickness as COTS surface arrays. By keeping the polyimide layer extremely thin, the microfabricated cortical device remains flexible enough to easily conform to the surface of the cortex which helps to limit the distance between electrode and neural activity. The ability for the microfabricated surface array to conform to the surface of the cortex is also aided by uniform array stiffness across its surface. This stems from the flexibility of the array resulting from the mechanical properties of the silicone and the polyimide and that the metal layers were relatively evenly distributed throughout the body of the array. Though COTS surface arrays are similar in thickness and material set to the microfabricated surface arrays, the bulk metal electrodes of COTS arrays (approximately 50 μm thick), lead to stiff regions that impede conformal contact with the cortex. Furthermore, in the arrays described here, the flexibility resulting from keeping the polyimide layer extremely thin also allows us to process the initially flat devices into 3D structures to achieve various mechanical characteristics. By bending the array around thermoplastic tubing and bonding it in place, the microfabricated depth array is transformed from a flexible 2D structure to a cylinder that is rigid enough for insertion into the brain. While previous work demonstrates two different methods for wrapping a grid array into a cylinder [39, 40], the present work is the first time a multilayer approach is used. This increases the available surface area for the electrodes while maximizing the available space for interconnects (metal traces) such that they can be placed underneath electrodes. Furthermore, the design here also allows for the integration of a central hollow lumen to allow a stylet or mandrel to be inserted if desired, modulating device stiffness.

An additional critical benefit of the thin-film microfabrication process is the combination of repeatability and design flexibility. Recent advances have introduced segmented depth leads to enable electric field steering and radial sensing [41, 42]. The thin-film microfabrication processes described above allow for highly custom designs to meet the needs of individual use cases [43]. Arrays can be designed with arbitrary electrode layout and density, and afterwards undergo post-processing to form the device into a depth probe. The combination of increased density and segmented electrodes can further improve the accuracy of stimulation and resolution of sensing in multiple radial directions and along the length of the probe.

4.2. Benefits for sensing

The findings presented here compliment and extend prior work in several ways. Previous studies in humans have tested ECoG arrays manufactured using standard platinum microwire techniques of greater density than COTS arrays: 3 mm pitch arrays were used

to link neural signals to individual and synergistic finger movements [44] and decode control of individual prosthetic fingers [45]; 4 mm pitch arrays were used to map speech processing in human nonprimary auditory cortex [46]. Recordings on adjacent 4 mm pitch electrodes showed raw local field potential correlations coefficients of 0.6, with significantly lower correlations during speech~task periods compared to non-task periods [19]. In the present study, we show that adjacent contacts at 2 mm pitch still provide unique information, even when recording during rest periods in absence of a task. This finding was robust across individuals, indicative of consistent high-quality recording using the fabricated thin-film arrays.

A number of studies using PEDOT:PSS arrays have also demonstrated that increased density of human brain surface recordings are beneficial; arrays with 0.4 mm pitch were superior to lower density arrays at classifying task conditions from neural activity alone [47]; 0.4 mm pitch arrays demonstrated frequency-specific spatial correlations, with spatially structured activity down to the sub-millimeter scale [48, 49]; PEDOT:PSS electrodes with 50–800 μm pitch were able to detect novel microscale events recorded from the surface of human cortex [50]. Arrays have been manufactured and tested with inter-electrode spacing as small as 23 μm, as with NeuroGrid arrays (23 μm inter-electrode spacing; tetrodes at 2 mm intervals) [51].

4.3. Benefits for stimulation

We demonstrated that higher spatial control of stimulation can be used to target the effects of stimulation. Single pulses of electrical stimulation have been used in a variety of applications to study CCEPs. These stimulation evoked responses represent causal local and distant responses that depend on the effective connectivity between the stimulated region and the site of recording. CCEPs have been used to assess functional network organization [52–54], potentiation and suppression of cortical activity induced by continuous stimulation [55], and to aid determination of epileptogenic zones from healthy regions [56, 57]. In this study, we measured CCEPs local to the stimulation contacts to characterize how the spacing of the stimulation contacts themselves influences the evoked responses. We found that the area of activated tissue, indicated by amplitude of evoked responses, varied depending on the proximity of the two stimulation electrodes. Studies often treat the stimulation location as a singular entity, but in practice stimulation is typically delivered between a bipolar electrode pair. The distance between the electrode contacts of that bipolar pair may fundamentally change the spread of current (and thus the neural population activated), resulting in different patterns of CCEPs in local and distant areas. While effective connectivity represented by CCEPs can change over time or as a function of intervention, we would not expect marked changes in effective connectivity during our experiments between the administration of SPS using the different electrode contacts. Therefore, we can interpret differences in locally evoked CCEPs as resulting from the current flow and tissue activated based on the distance between the stimulation contacts.

Prior human studies have also demonstrated the value in delivering more spatially precise intracortical stimulation. By using arrays of individual penetrating probes, stimulation was applied to precise regions of somatosensory cortex in order to evoke tactile sensations felt

coming from specific areas of the hand in a paralyzed individual [58] or in the arm of a tetraplegic individual [59]. However, the recording span of these electrode arrays is vastly smaller (2.4 mm × 4 mm), and the penetration by all contacts is a more× invasive implant.

4.4. The future of high-density μECOG and iEEG

While increasing density over current COTS arrays has been shown to be beneficial for sense and stimulation, there is an upper limit on utility of increasing μECoG and iEEG array density and decreasing contact sizes. Impedances increase and SNR ratio decrease with smaller contact size. Theoretically, at some point, adjacent contacts would have such highly correlated activity that no new information is gained. However, our results demonstrate that we have not yet reached this point. Work using recordings from both humans and animal models indicate that sub-millimeter electrode spacing is advantageous across a variety of cortical areas and frequency bands of interest, indicating continued miniaturization should continue [60]. Furthermore, research continues to optimize array geometry in terms of contact diameter vs pitch [33].

New materials and processes are being investigated and tested for μECoG arrays [51, 61–64], particularly with an eye towards reducing immune system activation. Ideally, novel arrays would incorporate biocompatible materials, reproducible manufacturing and assembly techniques, and provide high SNR recordings and stimulation capabilities. Arrays may increasingly have electronics included on or near the device in order to amplify, digitize, and multiplex signals and reduce the need for independent wires [65, 66]. Multiple emerging applications for intracranial sense and stimulation require sub-chronic (<30 d) or chronic (>30 d) implant. Additional testing and regulatory approval of thin-film arrays such as those described here will be required prior to this extended duration use, in particular to ensure mechanical stability and lack of any delamination [67]. In order for arrays to obtain FDA approval for human clinical use, arrays must be manufactured to meet quality control standards in sufficient quantity.

5. Conclusion

Subdural surface μECoG and iEEG depth arrays fabricated using thin-film microfabrication provide a robust and reproducible process for generating human-grade arrays for increased spatial resolution for neural sensing and stimulation.

Acknowledgments

The authors are grateful to members of the Chang Lab for assistance in conducting experiments and members of the SUBNETS team for productive discussion. This research was partially funded by the Defense Advanced Research Projects Agency (DARPA) under Cooperative Agreement No. W911NF-14-2-0043, issued by the Army Research Office contracting office in support of DARPA'S SUBNETS program. The views, opinions, and/or findings expressed are those of the author(s) and should not be interpreted as representing the official views or policies of the Department of Defense or the US Government.

Data availability statement

The data that support the findings of this study are available upon reasonable request from the authors.

References

[1]. Ferńandez IS and Loddenkemper T 2013 Electrocorticography for seizure foci mapping in epilepsy surgery J. Clin. Neurophysiol 30 554–70 [PubMed: 24300981]

[2]. Wellmer J, Von Der Groeben F, Klarmann U, Weber C, Elger CE, Urbach H, Clusmann H and Von Lehe M 2012 Risks and benefits of invasive epilepsy surgery workup with implanted subdural and depth electrodes Epilepsia 53 1322–32 [PubMed: 22708979]

[3]. Jobst BC, Bartolomei F, Diehl B, Frauscher B, Kahane P, Minotti L, Sharan A, Tardy N, Worrell G and Gotman J 2020 Intracranial EEG in the 21st century Epilepsy Curr. 20 180–8 [PubMed: 32677484]

[4]. Schalk G and Leuthardt EC 2011 Brain-computer interfaces using electrocorticographic signals IEEE Rev. Biomed. Eng 4 140–54 [PubMed: 22273796]

[5]. Yanagisawa T, Hirata M, Saitoh Y, Goto T, Kishima H, Fukuma R, Yokoi H, Kamitani Y and Yoshimine T 2011 Real-time control of a prosthetic hand using human electrocorticography signals J. Neurosurg 114 1715–22 [PubMed: 21314273]

[6]. Hartmann CJ, Fliegen S, Groiss SJ, Wojtecki L and Schnitzler A 2019 An update on best practice of deep brain stimulation in Parkinson's disease Ther. Adv. Neurol. Disord 12 175628641983809

[7]. Lee DJ, Lozano CS, Dallapiazza RF and Lozano AM 2019 Current and future directions of deep brain stimulation for neurological and psychiatric disorders: JNSPG 75th anniversary invited review article J. Neurosurg 131 333–42 [PubMed: 31370011]

[8]. Zangiabadi N, Ladino LD, Sina F, Orozco-Herńandez JP, Carter A and Téllez-Zenteno JF 2019 Deep brain stimulation and drug-resistant epilepsy: a review of the literature Front. Neurol 10 1–18 [PubMed: 30761061]

[9]. Hamberger MJ 2007 Cortical language mapping in epilepsy: a critical review Neuropsychol. Rev 17 477–89 [PubMed: 18004662]

[10]. Parastarfeizabadi M and Kouzani AZ 2017 Advances in closed-loop deep brain stimulation devices *J.* Neuroeng. Rehabil 14 79

[11]. Lo M-C and Widge AS 2017 Closed-loop neuromodulation systems: next-generation treatments for psychiatric illness Int. Rev. Psychiatry Abingdon. Engl 29 191–204

[12]. Chang EF 2015 Towards large-scale, human-based, mesoscopic neurotechnologies Neuron 86 68–78 [PubMed: 25856487]

[13]. Muller L, Felix S, Shah KG, Lee K, Pannu S and Chang EF 2016 Thin-film, high-density micro-electrocorticographic decoding of a human cortical gyrus Annu. Int. Conf. IEEE Eng. Med. Biol. Soc 2016 1528–31 [PubMed: 28268617]

[14]. Rubehn B, Bosman C, Oostenveld R, Fries P and Stieglitz T 2009 A MEMS-based flexible multichannel ECoG-electrode array J. Neural Eng 6 036003 [PubMed: 19436080]

[15]. Diaz-Botia CA, Luna LE, Neely RM, Chamanzar M, Carraro C, Carmena JM, Sabes PN, Maboudian R and Maharbiz MM 2017 A silicon carbide array for electrocorticography and peripheral nerve recording J. Neural Eng 14 056006 [PubMed: 28573982]

[16]. Rousche PJ, Pellinen DS, Pivin DP, Williams JC, Vetter RJ and Kipke DR 2001 Flexible polyimide-based intracortical electrode arrays with bioactive capability IEEE Trans. Biomed. Eng 48 361–71 [PubMed: 11327505]

[17]. Wang PT et al. 2016 Comparison of decoding resolution of standard and high-density electrocorticogram electrodes J. Neural Eng 13 026016 [PubMed: 26859341]

[18]. Kellis S, Sorensen L, Darvas F, Sayres C, O'Neill K, Brown RB, House P, Ojemann J and Greger B 2016 Multi-scale analysis of neural activity in humans: implications for micro-scale electrocorticography Clin. Neurophysiol 127 591–601 [PubMed: 26138146]

[19]. Muller L, Hamilton LS, Edwards E, Bouchard KE and Chang EF 2016 Spatial resolution dependence on spectral frequency in human speech cortex electrocorticography J. Neural Eng 13 056013 [PubMed: 27578414]

[20]. Chiang C-H, Lee J, Wang C, Williams AJ, Lucas TH, Cohen YE and Viventi J 2020 A modular high-density μECoG system on macaque vlPFC for auditory cognitive decoding J. Neural Eng 17 046008 [PubMed: 32498058]

[21]. Kaiju T, Doi K, Yokota M, Watanabe K, Inoue M, Ando H, Takahashi K, Yoshida F, Hirata M and Suzuki T 2017 High spatiotemporal resolution ecog recording of somatosensory evoked potentials with flexible micro-electrode arrays Front. Neural Circuits 11 1–13 [PubMed: 28174523]

[22]. Rossetti N, Hagler J, Kateb P and Cicoira F 2021 Neural and electromyography PEDOT electrodes for invasive stimulation and recording J. Mater. Chem. C 9 7243–63

[23]. Cui XT and Zhou DD 2007 Poly (3,4-ethylenedioxythiophene) for chronic neural stimulation IEEE Trans. Neural Syst. Rehabil. Eng 15 502–8 [PubMed: 18198707]

[24]. Green RA, Hassarati RT, Bouchinet L, Lee CS, Cheong GLM, Yu JF, Dodds CW, Suaning GJ, Poole-Warren LA and Lovell NH 2012 Substrate dependent stability of conducting polymer coatings on medical electrodes Biomaterials 33 5875–86 [PubMed: 22656446]

[25]. Ivanovskaya AN, Belle AM, Yorita AM, Qian F, Chen S, Tooker A, Lozada RG, Dahlquist D and Tolosa V 2018 Electrochemical roughening of thin-film platinum for neural probe arrays and biosensing applications J. Electrochem. Soc 165 G3125

[26]. Sun Y, Lacour SP, Brooks RA, Rushton N, Fawcett J and Cameron RE 2009 Assessment of the biocompatibility of photosensitive polyimide for implantable medical device use J. Biomed. Mater. Res. A 90 648–55 [PubMed: 18563817]

[27]. Constantin CP, Aflori M, Damian RF and Rusu RD 2019 Biocompatibility of polyimides: a mini-review Materials 12 3166 [PubMed: 31569679]

[28]. Tooker A et al. 2012 Optimization of multi-layer metal neural probe design Annu. Int. Conf. IEEE Eng. Med. Biol. Soc 2012 5995–8 [PubMed: 23367295]

[29]. Stieglitz T, Beutel H, Schuettler M and Meyer J-U 2000 Micromachined, polyimide-based devices for flexible neural interfaces Biomed. Microdevices 2 283–94

[30]. Sylwestrowicz WD, Elkholy HA and Kammlott GW 1979 The effect of temperature and humidity on interdiffusion of gold and titanium in thin films J. Mater. Sci 14 873–81

[31]. Martinez WE, Gregori G and Mates T 2010 Titanium diffusion in gold thin films Thin Solid Films 518 2585–91

[32]. Masahiro K and Noboru S 1993 Effects of temperature, thickness and atmosphere on mixing in Au-Ti bilayer thin films J. Mater. Sci 28 5088–91

[33]. Wang X, Gkogkidis CA, Iljina O, Fiederer LDJ, Henle C, Mader I, Kaminsky J, Stieglitz T, Gierthmuehlen M and Ball T 2017 Mapping the fine structure of cortical activity with different micro-ECoG electrode array geometries J. Neural Eng 14 056004 [PubMed: 28597847]

[34]. Lvovich V 2012 Impedance-spectroscopy modifications Impedance Spectroscopy: Applications to Electrochemical and Dielectric Phenomena (New York: Wiley) pp 319–31

[35]. Petrossians A, Whalen JJ, Weiland JD and Mansfeld F 2011 Electrodeposition and characterization of thin-film platinum-iridium alloys for biological interfaces J. Electrochem. Soc 158 D269

[36]. Stieglitz T 2020 Of man and mice: translational research in neurotechnology Neuron 105 12–15 [PubMed: 31951526]

[37]. Cogan SF, Ludwig KA, Welle CG and Takmakov P 2016 Tissue damage thresholds during therapeutic electrical stimulation J. Neural Eng 13 021001 [PubMed: 26792176]

[38]. Sellers KK, Schuerman WL, Dawes HE, Chang EF and Leonard MK 2019 Comparison of common artifact rejection methods applied to direct cortical and peripheral stimulation in human ECoG: 2019 9th Int. IEEE/EMBS Conf. on Neural Engineering (NER) p 77–80

[39]. Fomani AA, Mansour RR, Florez-Quenguan CM and Carlen PL 2011 Development and characterization of multisite three-dimensional microprobes for deep brain stimulation and recording J. Microelectromech. Syst 20 1109–18

[40]. Pothof F, Bonini L, Lanzilotto M, Livi A, Fogassi L, Orban GA, Paul O and Ruther P 2016 Chronic neural probe for simultaneous recording of single-unit, multi-unit, and local field potential activity from multiple brain sites J. Neural Eng 13 046006 [PubMed: 27247248]

[41]. Steigerwald F, Müller L, Johannes S, Matthies C and Volkmann J 2016 Directional deep brain stimulation of the subthalamic nucleus: a pilot study using a novel neurostimulation device Mov. Disorders 31 1240–3

[42]. Aman JE et al. 2020 Directional deep brain stimulation leads reveal spatially distinct oscillatory activity in the globus pallidus internus of Parkinson's disease patients Neurobiol. Dis 1 104819

[43]. Kim C, Jeong J and Kim SJ 2019 Recent progress on non-conventional microfabricated probes for the chronic recording of cortical neural activity Sensors 19 5

[44]. Kuo C-H, Blakely TM, Wander JD, Sarma D, Wu J, Casimo K, Weaver KE and Ojemann JG 2019 Context-dependent relationship in high-resolution micro-ECoG studies during finger movements J. Neurosurg 132 1358–66 [PubMed: 31026831]

[45]. Hotson G et al. 2016 Individual finger control of a modular prosthetic limb using high-density electrocorticography in a human subject J. Neural Eng 13 026017 [PubMed: 26863276]

[46]. Pasley BN, David SV, Mesgarani N, Flinker A, Shamma SA, Crone NE, Knight RT and Chang EF 2012 Reconstructing speech from human auditory cortex PLoS Biol. 10 e1001251 [PubMed: 22303281]

[47]. Hermiz J, Rogers N, Kaestner E, Ganji M, Cleary DR, Carter BS, Barba D, Dayeh SA, Halgren E and Gilja V 2018 Sub-millimeter ECoG pitch in human enables higher fidelity cognitive neural state estimation Neuroimage 1 454–64

[48]. Rogers N et al. 2019 Correlation structure in micro-ECoG recordings is described by spatially coherent components PLoS Comput. Biol 15 e1006769 [PubMed: 30742605]

[49]. Ganji M et al. 2018 Development and Translation of PEDOT:PSS microelectrodes for intraoperative monitoring Adv. Funct. Mater 28 1700232

[50]. Paulk AC et al. 2021 Microscale physiological events on the human cortical surface Cereb. Cortex 31 3678–700 [PubMed: 33749727]

[51]. Khodagholy D, Gelinas JN, Zhao Z, Yeh M, Long M, Greenlee JD, Doyle W, Devinsky O and Buzśaki G 2016 Organic electronics for high-resolution electrocorticography of the human brain Sci. Adv 2 e1601027 [PubMed: 28861464]

[52]. Keller CJ, Honey CJ, Entz L, Bickel S, Groppe DM, Toth E, Ulbert I, Lado FA and Mehta AD 2014 Corticocortical evoked potentials reveal projectors and integrators in human brain networks J. Neurosci 34 9152–63 [PubMed: 24990935]

[53]. Dionisio S, Mayoglou L, Cho S-M, Prime D, Flanigan PM, Lega B, Mosher J, Leahy R, Gonzalez-Martinez J and Nair D 2019 Connectivity of the human insula: a cortico-cortical evoked potential (CCEP) study Cortex 1 419–42

[54]. Matsumoto R, Nair DR, LaPresto E, Bingaman W, Shibasaki H and Lüders HO 2007 Functional connectivity in human cortical motor system: a cortico-cortical evoked potential study Brain J. Neurol 130 181–97

[55]. Keller CJ, Huang Y, Herrero JL, Fini ME, Du V, Lado FA, Honey CJ and Mehta AD 2018 Induction and quantification of excitability changes in human cortical networks J. Neurosci 38 5384–98 [PubMed: 29875229]

[56]. Zhao C et al. 2019 Localization of epileptogenic zone based on cortico-cortical evoked potential (CCEP): a feature extraction and graph theory approach Front. Neuroinf 13 1–9

[57]. Zhang N et al. 2018 The effectiveness of cortico-cortical evoked potential in detecting seizure onset zones Neurol. Res 40 480–90 [PubMed: 29575990]

[58]. Flesher SN, Collinger JL, Foldes ST, Weiss JM, Downey JE, Tyler-Kabara EC, Bensmaia SJ, Schwartz AB, Boninger ML and Gaunt RA 2016 Intracortical microstimulation of human somatosensory cortex Sci. Transl. Med 8 361ra141–361ra141

[59]. Armenta Salas M et al. 2018 Proprioceptive and cutaneous sensations in humans elicited by intracortical microstimulation eLife 10 e32904

[60]. Trumpis M et al. 2020 Sufficient sampling for kriging prediction of cortical potential in rat, monkey, and human μECoG J. Neural Eng 18 036011

[61]. Shokoueinejad M et al. 2019 Progress in the field of micro-electrocorticography Micromachines 10

[62]. Kim D-H et al. 2010 Dissolvable films of silk fibroin for ultrathin conformal bio-integrated electronics Nat. Mater 9 511–7 [PubMed: 20400953]

[63]. Ledochowitsch P, Koralek AC, Moses D, Carmena JM and Maharbiz MM 2013 Sub-mm functional decoupling of electrocortical signals through closed-loop BMI learning Annu. Int. Conf. IEEE Eng. Med. Biol. Soc 2013 5622–5 [PubMed: 24111012]

[64]. Massey TL, Santacruz SR, Hou JF, Pister KSJ, Carmena JM and Maharbiz MM 2019 A high-density carbon fiber neural recording array technology J. Neural Eng 16 016024 [PubMed: 30524060]

[65]. Viventi J et al. 2011 Flexible, foldable, actively multiplexed, high-density electrode array for mapping brain activity *in vivo* Nat. Neurosci 14 1599–605 [PubMed: 22081157]

[66]. Chiang C-H et al. 2021 Flexible, high-resolution thin-film electrodes for human and animal neural research J. Neural Eng 18 045009

[67]. Čvančara P et al. 2020 Stability of flexible thin-film metallization stimulation electrodes: analysis of explants after first-in-human study and improvement of in vivo performance J. Neural Eng 17 046006 [PubMed: 32512544]

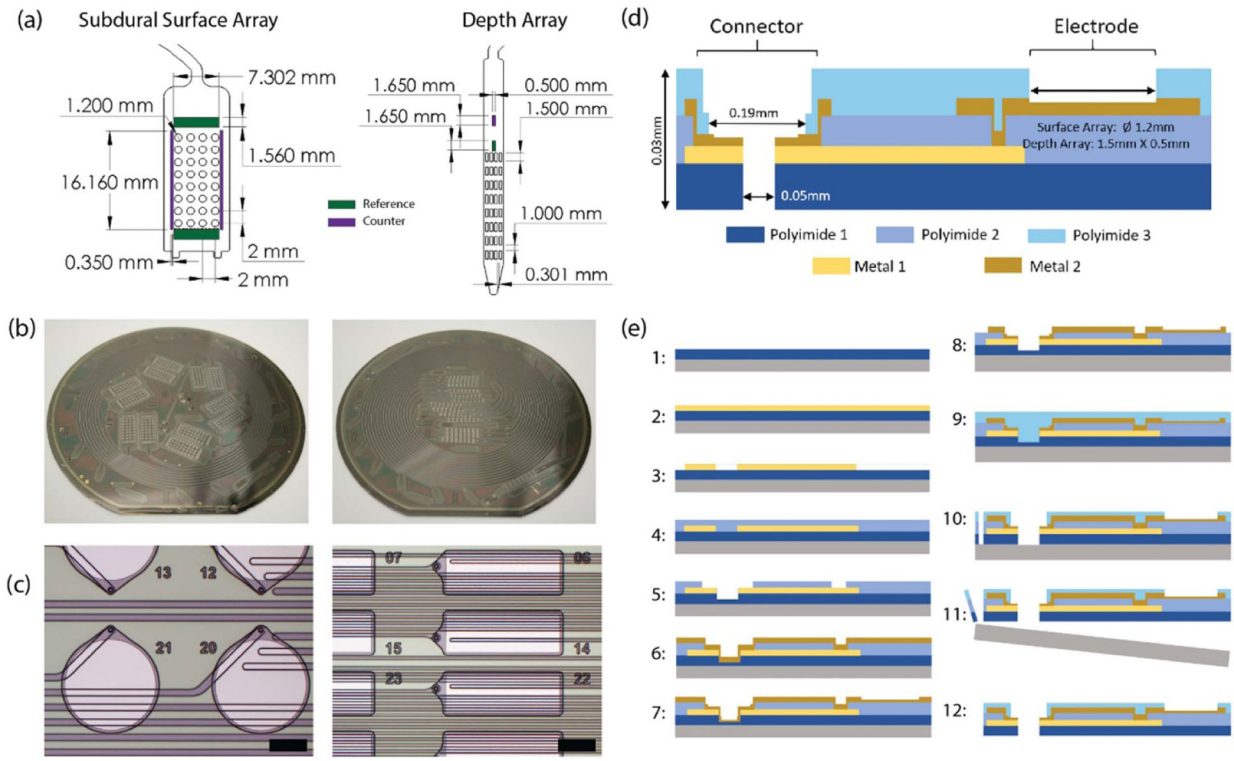

Figure 1.

Surface and depth array design and manufacture. Surface and depth arrays consist of (a) 32 PtIr electrodes that span a region of 15.2 mm × 7.2 mm and 19 mm × 2.9 mm (when laid flat), respectively, with surface array electrodes of 1.2 mm diameter and the depth array electrodes dimensions of 1.5 mm × 0.5 mm. Both arrays have a set of counter and reference electrodes (colored in purple and green, respectively; on surface arrays the two reference electrodes were electrically shorted thereby increasing the surface area used for reference; same for the two counter electrodes). (b) Twelve arrays were fabricated on each silicon carrier with the cables tiled radially in a spiral layout to assist coiling during device assembly, maintain elasticity and length, and increase kink resistance. (c) Optical image of the electrode region showing electrical traces run underneath the electrodes; the topography of the electrode contact does not hinder its performance. Scale bars represent 0.5 mm. (d) Cross-sectional schematic of both arrays illustrating the two Ti/PtIr/Au/PtIr/Ti metal layers (each 2.04 μm thick) separated by a 10 μm thick insulative polymer, polyimide. (e) Process flow of the fabrication steps for both type of arrays: (e.1) polyimide spin-coated and cured on a silicon wafer, (e.2) first metal layer deposited, (e.3) metal layer patterned via plasma etch process, (e.4) polyimide spin-coated and cured to insulate first metal layer, (e.5) interconnection vias patterned on polyimide to enable electrical contact with next metal layer, (e.6) second metal layer deposited, (e.7) top titanium layer removed from connector and electrode region to expose underlying PtIr surface, (e.8) second metal layer patterned, (e.9) polyimide spin-coated and cured, (e.10) polyimide patterned to expose connector/electrode surfaces and device outline, and finally, (e.11) the wafer was soaked in warm water and devices were peeled to (e.12) release the flexible device.

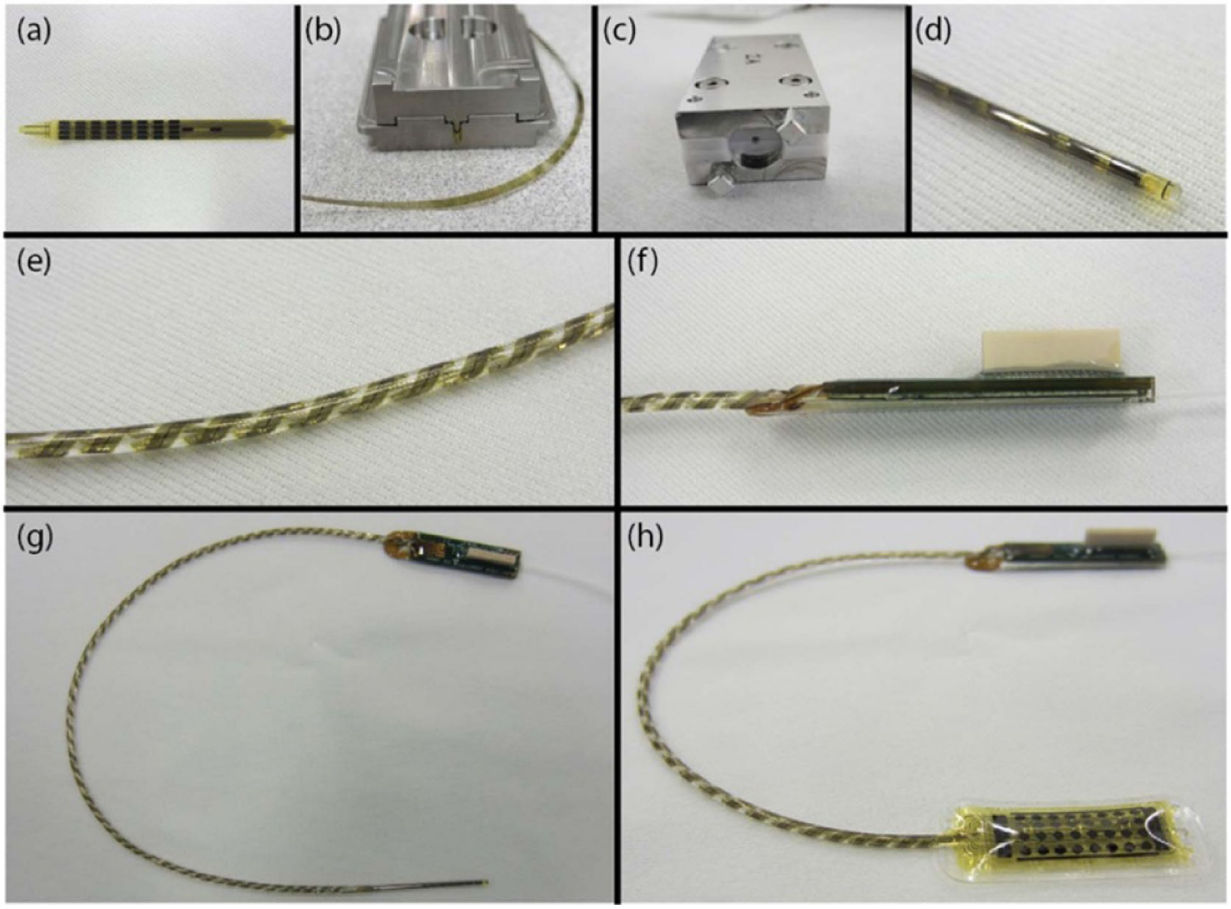

Figure 2.

Assembly and post-fabrication modifications to arrays. After being removed from the carrier wafer, surface and depth arrays underwent several post-fabrication processing steps. Steps (a)–(d) apply to depth arrays only: (a) the flat depth array was heated to 260 °C and formed into a 'U' shape using a stainless-steel forming tool (b). Once cooled, the forming tool was removed and the pointed array tip was temporarily bonded to a thermoplastic polyurethane (TPU) support tube using UV-cure adhesive. (c) The 'U' shaped device was then pulled through a polytetrafluoroethylene forming tool to form it into a cylinder; the mold was heated to 150 °C to reflow the TPU which permanently bonds the array to the support tube. (d) A rounded tip was then formed at the end of the array. (e) For both the surface and depth arrays, the cable region of the device was helically wound around the support tube and over-molded in silicone. (f) The interface board was then molded in biocompatible epoxy. Fully fabricated and assembled depth array (g) and surface array (h)—surface array may also be over-molded in silicone.

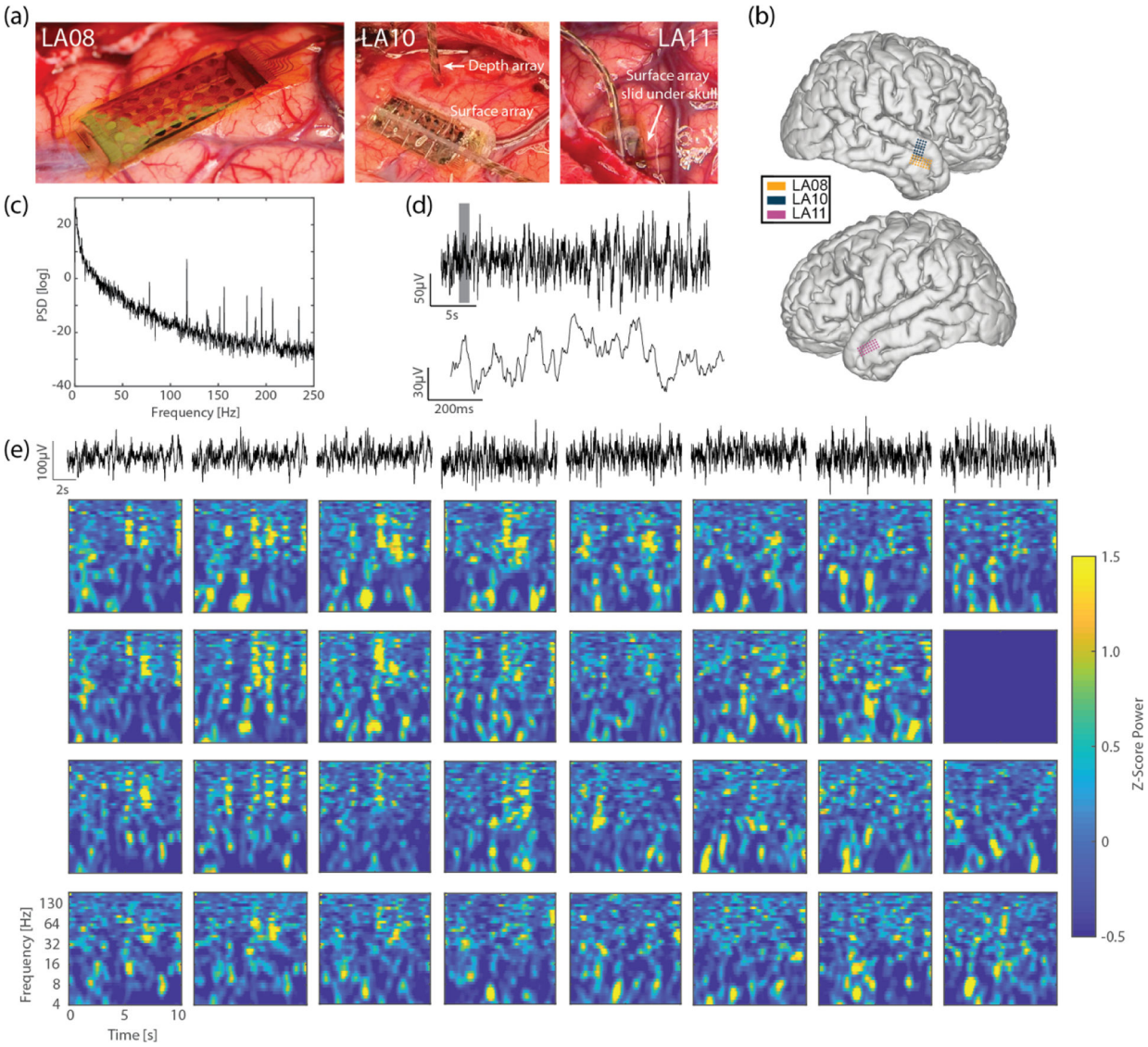

Figure 3.

Intraoperative human testing of thin-film μECoG and iEEG arrays. (a) Intraoperative array placements in LA08, LA10, and LA11. (b) Rendering of right hemisphere (top) and left hemisphere (bottom) with color-coded approximate locations of surface array placement for participants, all placed over the anterior temporal lobe with differing degrees of coverage of the middle temporal gyrus and superior temporal gyrus. In patients where depth electrodes were placed, they were also placed within the anterior temporal lobe. (c) Power spectral density plot of raw data from channel 1 of LA08. (d) Time domain traces from channel 1 of LA08. Time shown in bottom plot corresponds to shaded area in top plot. (e) Preprocessed time domain traces and spectrograms taken from 10 s of resting state recording in LA08. Subplots organized according to surface array organization, with channel 1 in the top left corner; time domain traces correspond to spectrograms in the top row.

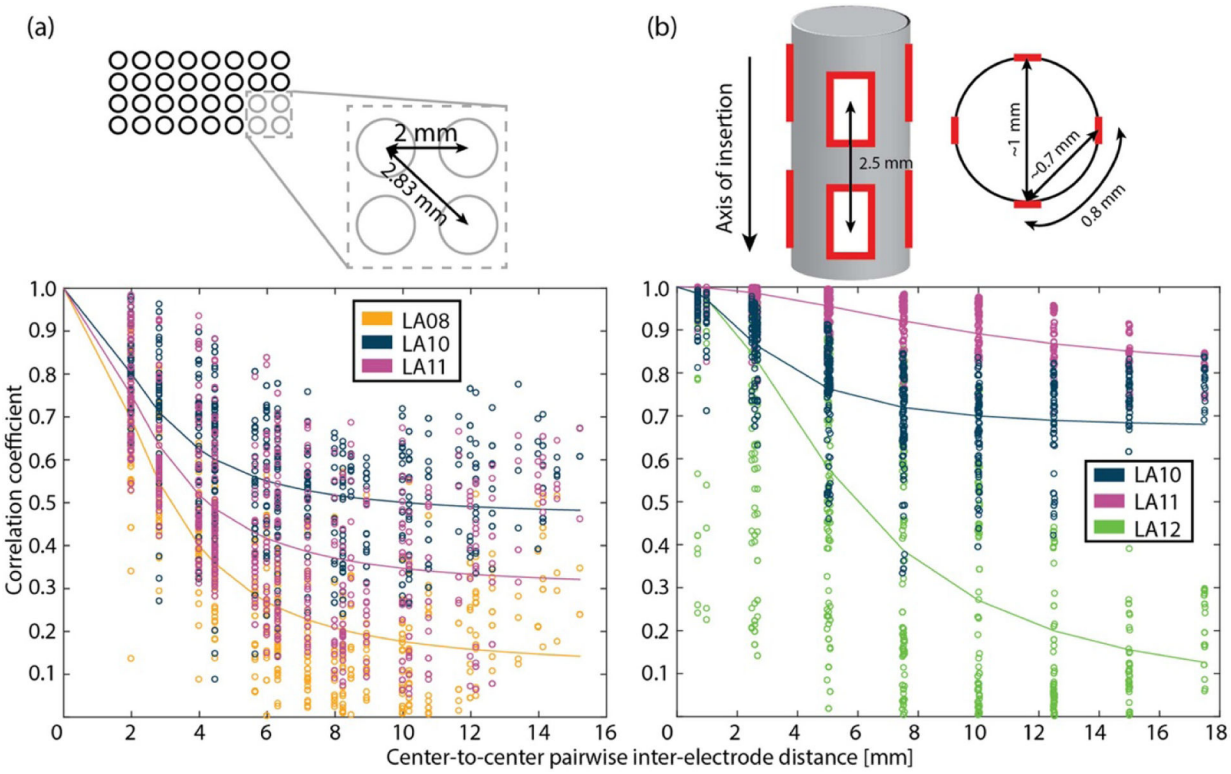

Figure 4.

Inter-electrode correlations decrease over distance. (a) Top: Euclidean center-to-center inter-electrode distances were calculated on the surface array; neighboring horizontal and vertical contacts are separated by 2 mm while the next closest contacts on the diagonal are separated by ~2.83 mm. Bottom: pair-wise Pearson correlation coefficient was calculated between all electrode pairs (*y*-axis) using pre-stimulation baseline data and fit to a Lorentzian (1) function of the inter-electrode distance (*x*-axis, mm). (b) Depth arrays: top, schematic depicting a subsegment of the depth array with electrode contacts outlined in red. Euclidean center-to-center inter-electrode distances were calculated among all depth arrays as estimated as a three-dimensional surface. The closest neighboring contacts are at the same depth of insertion are separated by ~0.7 mm and 1 mm, with the closest contacts at a different depth at a center-to-center distance of 2.5 mm. Bottom, same as (a) bottom, with ~the pairwise Pearson correlation coefficient (*y*-axis) plotted against inter-electrode Euclidean distance (*x*-axis, mm), fit using a Lorentzian regression model (1).

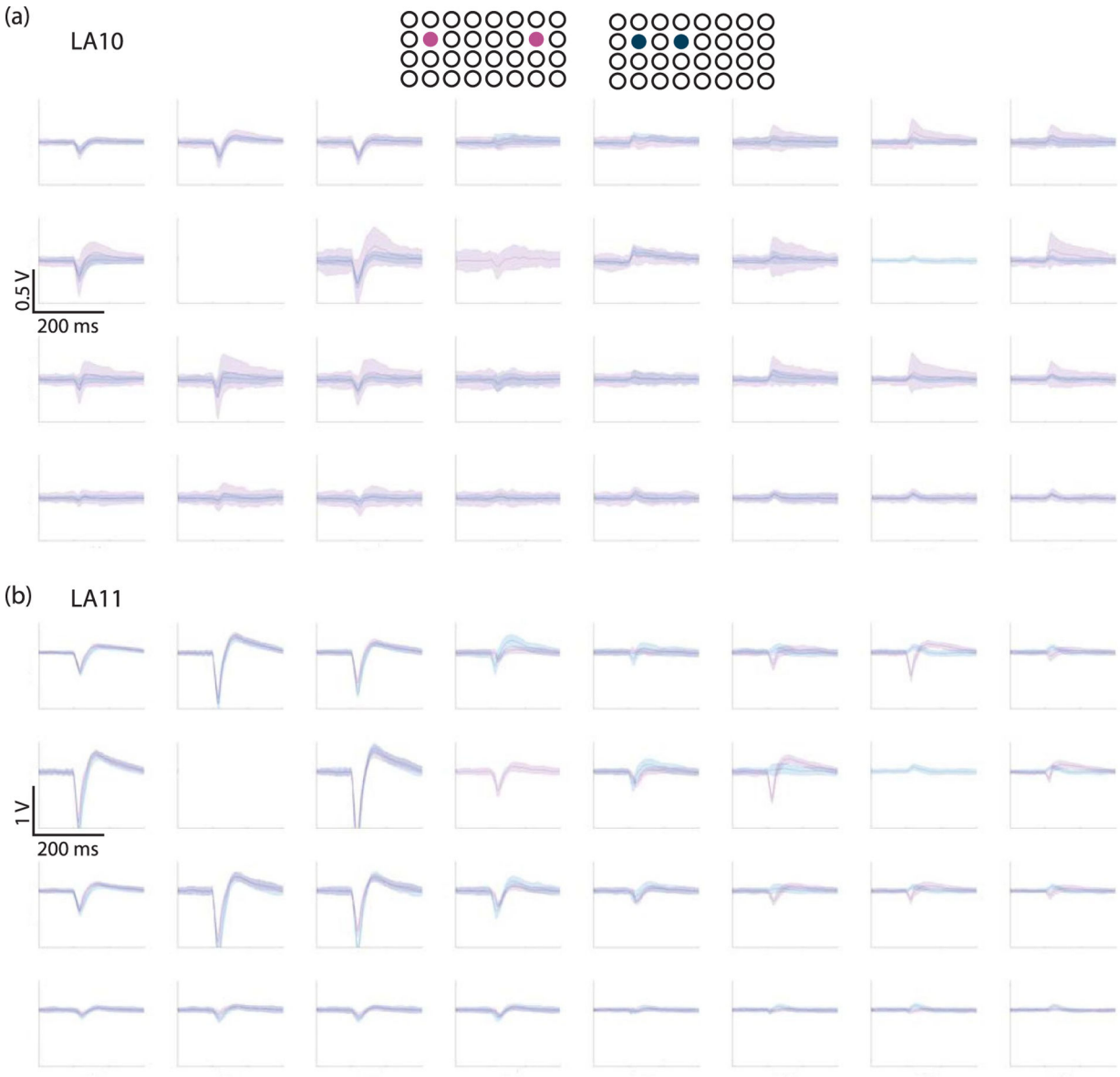

Figure 5.

SPS administered with different bipolar inter-electrode distances changes evoked potentials. (a) Top, schematics of surface arrays with contacts as circles and stimulation electrodes at 10 mm center-to-center distance highlighted in purple (left) or 4 mm center-to-center distance highlighted in blue (right). Below, average SPS-evoked voltage potentials 1 standard deviation for participant LA10, shown in geometric distribution of electrode contacts corresponding to above array±schematics. Colors correspond to above schematics. 300 ms data plotted, with stimulation occurring at 100 ms. Scalebar insert. (b) Same as (a), but for participant LA11.

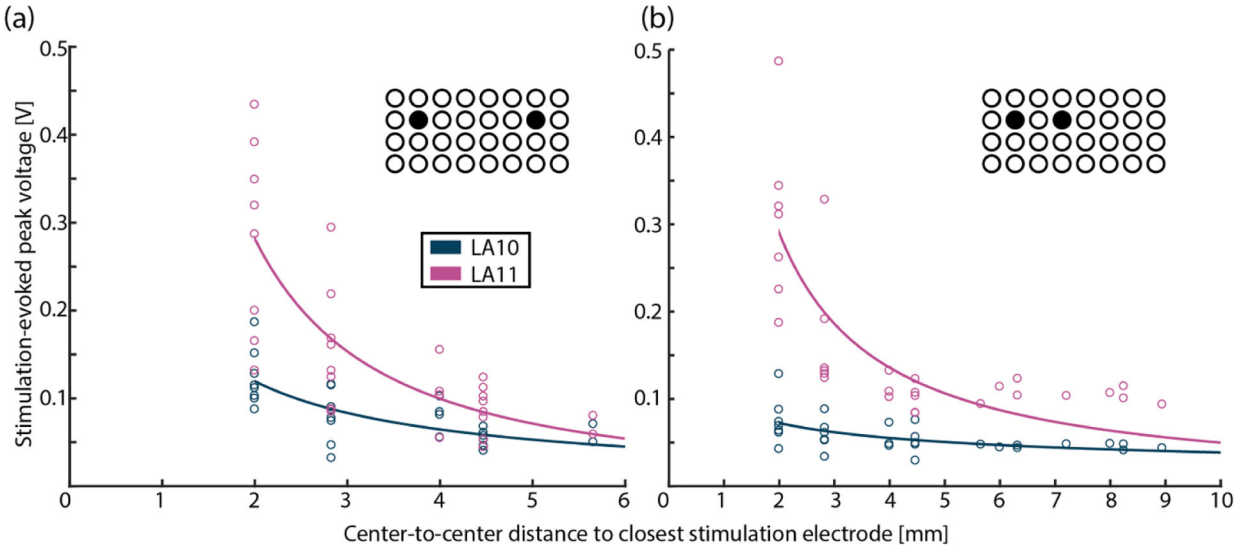

Figure 6.

SPS-evoked potential peak decreases with distance from stimulation sites. (a) SPS peak responses by distance for 10 mm spaced electrodes. *Y*-axis, stimulation evoked peak voltage; *x*-axis, center-to-center distance to closest stimulation electrode in mm, with average peak for each recording electrode for each participant shown as an open circle, and fit power relationship (2) as line. (b) Same as (a), but for stimulation electrodes with 4 mm center-to-center spacing.

Table 1.

Materials selection, manufacturability, and known compliance.

Material	Manufacturability	Known compliance (if any)
Polyimide PI-2611 (HD Microsystems)	Widely available	Various studies, e.g. [26, 27]
Loctite 4310 (Henkel Adhesives)	Widely available	Meets ISO 10993 per vendor
EpoTek 301–2FL (Epoxy Technology)	Widely available	Meets ISO 10 993 per vendor
EpoTek 301–2 (Epoxy Technology)	Widely available	Meets ISO 10 993 per vendor
AlliedSil Silicone Tubing—Implant Grade (Implantech)	Widely available	Indicated by vendor for use in chronic (⩾30 d) implant applications, 510(k) # K955433
Carbothane TPU PC-3585 A (Lubrizol Corporation)	Widely available	Indicated by vendor for use in chronic (⩾30 d) implant applications
Nusil MED-6215 (Avantor, Inc)	Widely available	Indicated by vendor for use in chronic (⩾30 d) implant applications, FDA Master File available

Table 2.

Participant information.

Participant	Age (years)	Gender	Side	Surgical indication	State	Anesthesia during recording	Surface array	Depth array
LA08	55	Female	Right	Epilepsy	Anesthetized	N_2O, dexmedetomidine, remifentanil	Yes	No
LA10	22	Male	Right	Epilepsy	Anesthetized	N_2O, dexmedetomidine, remifentanil	Yes	Yes
LA11	28	Female	Left	Epilepsy	Awake	Propofol and remifentanil held	Yes	Yes
LA12	29	Female	Right	Epilepsy	Anesthetized	during recording N_2O, dexmedetomidine, remifentanil	No	Yes